Frontiers in Heat and Mass Transfer

Tech Science Press

https://doi.org/10.32604/fhmt.2026.076455

ARTICLE

Transient Numerical Analysis of Carbon Monoxide Dispersion in Underground Spaces under Different Ventilation Conditions: A Localized Fire Scenario

M. I. Hernández-López[1], E. V. Macias-Melo[2], F. N. Demesa-López[1] and J. Serrano-Arellano[1,*]

[1]División de Estudios de Posgrado e Investigación, Tecnológico Nacional de México/IT de Pachuca, Carretera México-Pachuca km. 87.5, Colonia Venta Prieta, Pachuca de Soto, Hgo., México

[2]División Académica de Ingeniería y Arquitectura, Universidad Juárez Autónoma de Tabasco (DAIA-UJAT), Carretera Cunduacán-Jalpa de Méndez km. 1, Cunduacán, Tab., México

*Corresponding Author: J. Serrano-Arellano. Email: juan.sa@pachuca.tecnm.mx

Received: 21 November 2025; Accepted: 22 January 2026; Published: 30 April 2026

ABSTRACT: The accumulation of carbon monoxide (CO) in underground spaces poses a significant health hazard; therefore, effective ventilation is essential. This study presents a transient numerical analysis under turbulent flow conditions to evaluate CO dispersion, and identify optimal ventilation configurations. Both during normal operation and in scenarios with high localized concentrations, such as a fire event. The governing equations were solved using the finite volume method with the standard k–ε. Turbulence model. Three configurations were analyzed by varying the outlet location: Case A with an upper-left outlet, Case B with a mid-left outlet, and Case C with a lower-left outlet. The Reynolds number (Re) ranged from 500 to 10,000 to represent different flow velocities. The results showed that the time required to purge the interior region ranged from 11 to 16 s for Re = 5000 and Re = 10,000, achieving minimum average (CO) concentrations of 1 ppm. Case C exhibited cross-ventilation that enhanced contaminant removal, whereas Case A demonstrated the highest overall distribution efficiency (ε_C = 14.364). In the localized fire scenario, cross-ventilation minimized CO propagation into the interior, with removal times ranging from 11 to 191 s. This depended on the fire location and the Reynolds number. This study demonstrates that outlet positioning, flow velocity, and the presence of thermal plumes significantly influence CO dispersion and removal. The findings provide practical design and operational guidelines for ventilation systems in confined underground environments, ensuring occupant safety and maintaining indoor air quality during both normal and emergency conditions.

KEYWORDS: Numerical simulation; cross ventilation; carbon monoxide dispersion; localized fire; transient analysis

1 Introduction

Underground cities originally emerged for defensive, religious, military, or climatic reasons, representing remarkable achievements in engineering and human adaptation. From ancient shelters to modern urban projects, they demonstrate how societies have utilized the subsurface to address challenges related to safety, overpopulation, land use, and sustainability. Currently, the construction of underground infrastructures has increased in response to growing urban congestion. Beyond being an alternative to surface space limitations, underground construction offers multiple advantages: the stable subsurface temperature reduces heating and cooling demands, resulting in energy savings; it optimizes land use in densely populated cities; improves mobility through underground transportation systems; and provides protection against extreme weather events [1–4]. Common examples include subway stations, parking facilities, warehouses, shelters, and underground commercial areas. However, these infrastructures also pose challenges such as high construction

costs, complex planning requirements, safety risks (e.g., fires, flooding, or structural failures), and health issues associated with inadequate sunlight exposure or poor ventilation. One of the main challenges in such environments is air quality control, as the lack of natural ventilation promotes the accumulation of pollutants such as *CO*, CO_2, NO_2, *NO*x, volatile organic compounds (VOCs), particulate matter (PM), and radon [5–7]. Among these, carbon monoxide (CO) is particularly critical because it is colorless and odorless, and at high concentrations it can cause headaches, dizziness, severe poisoning, or even death [8,9]. Several studies have shown that ventilation effectiveness and air quality strongly depend on the configuration of inlets and outlets, flow rates, and the geometry of the space. Studies [10,11] demonstrated that contaminant extraction efficiency depends on the relative position of the source and ventilation openings. Reference [12] highlighted that the arrangement of ventilation directly influences thermal comfort and users' perception, whereas reference [13] demonstrated through computational fluid dynamics (CFD) simulations that inlet and outlet positioning, along with variable ventilation rates, significantly affect contaminant dispersion. Reference [14] confirmed that combined supply-and-exhaust systems enhance *CO* removal efficiency, while later studies [15,16] showed that obstacles and partition walls alter airflow circulation, impacting pollutant removal. Additional research [17–22] emphasized the importance of integrated ventilation and emission control strategies to maintain indoor air quality within WHO-recommended limits. Recent studies [23–26] have also highlighted that ventilation efficiency depends on the configuration of openings and ducts, flow rates, temperature gradients, and occupant distribution, underlining the need for proper ventilation system design and management. Regarding *CO* dispersion, studies [13,27] reported that air velocities around 2 m/s are effective in maintaining *CO* concentrations within safe limits. Reference [28] determined that a minimum ventilation rate of 3.5 ACH is required under normal conditions and up to 9.2 ACH under extreme conditions, while Ref. [14] reported CO concentrations ranging from 24 to 235 ppm, observing that combined supply-and-exhaust systems are more effective than exhaust-only systems. Subsequent investigations [29] confirmed that airflow velocity and distribution are key parameters for *CO* control, and studies [15,16] demonstrated that physical barriers require higher local velocities to achieve similar *CO* dispersion levels. Reference [30] showed that inclined single-jet fans improve *CO* dispersion, optimizing efficiency even at moderate flow velocities. Therefore, the design and operation of efficient ventilation systems are crucial to control internal *CO* and other pollutant concentrations in these environments [31,32]. An inadequate ventilation strategy not only reduces contaminant removal effectiveness but also increases the risk of occupant exposure [33]. The following studies have also addressed the thermal behavior and smoke propagation in confined environments such as underground car parks, tunnels, and coal mines, emphasizing the critical role of ventilation in the evolution of fires and the dispersion of pollutants. Studies [34,35] highlighted the vulnerability of these environments and the need for safe and efficient ventilation systems. Complementary experimental and numerical investigations [36–38] demonstrated that a localized vehicle fire can evolve rapidly and intensify depending on airflow velocity and direction. Full-scale experiments [39,40] confirmed that fire propagation to adjacent vehicles can occur within minutes, while CFD models [41] have been used to predict the thermal distribution, *CO* concentration, and smoke movement. Reference [42] analyzed smoke and *CO* behavior in underground car parks affected by vehicle fires using the Fire Dynamics Simulator (FDS), considering various geometric aspects and horizontal ventilation configurations. They observed that the heat release rate (HRR) can range from 0.5 to 20 MW, and that the sudden inflow of fresh air may reignite the fire, thereby increasing its severity. Localized fires or heat sources in underground spaces can drastically alter airflow patterns and pollutant dispersion. Experimental and numerical studies have shown that the interaction between thermal buoyancy and forced ventilation can reduce extraction efficiency [43–46]. Subsequent experimental and numerical research [47–51] demonstrated that the geometry of the car park and the arrangement of openings significantly influence smoke and *CO* propagation. Moreover, jet fan ventilation systems can disturb smoke stratification and increase *CO* concentrations at the occupied zone (~2 m height),

affecting both visibility and occupant safety. Nevertheless, a gap remains in transient numerical analyses of *CO* dispersion generated by localized fires under different ventilation strategies. This work aims to address this gap through transient CFD simulations focused on identifying configurations that minimize occupant exposure and maintain *CO* concentrations within OSHA limits [52] (9 ppm over 8 h; 25 ppm over 1 h).

Accordingly, the present study focuses on the transient analysis of *CO* dispersion in underground spaces under different ventilation conditions, including localized fire scenarios, using CFD under turbulent flow (k–ε model). The effects of inlet–outlet configuration and inlet velocity on contaminant dilution and dispersion are evaluated, providing practical guidelines for the design and operation of ventilation systems in tunnels and underground car parks. The results offer criteria for developing safer, more comfortable, and sustainable underground environments, considering energy efficiency and occupant health protection.

2 Physical Model

This section describes the physical model employed for the different study cases. The analyzed domain corresponds to a rectangular cavity in which three outlet configurations were evaluated, each located on the left wall: an upper outlet (Case A), a mid-height outlet (Case B), and a lower outlet (Case C), as shown in Fig. 1.

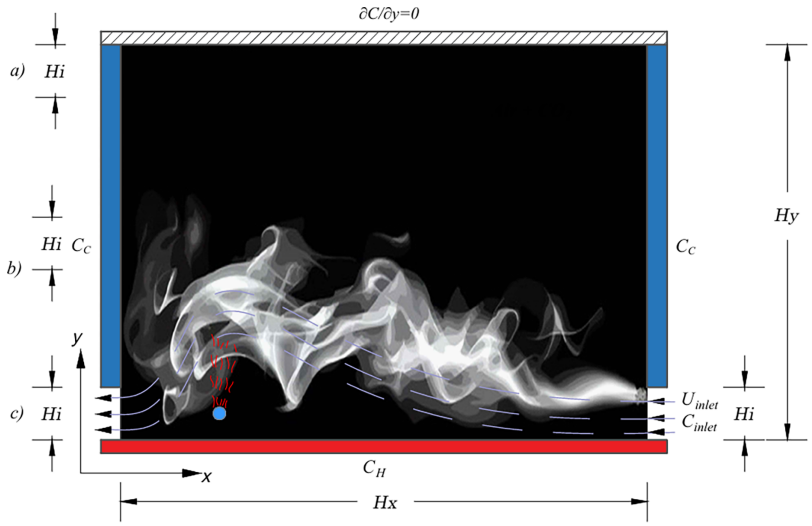

Figure 1: Physical model of the ventilated cavity with a contaminant source: localized fire.

Air enters through the left wall with a minimum carbon monoxide (*CO*) concentration of C_{inlet} = 1 ppm, corresponding to outdoor air. The inlet velocity was defined as a function of the Reynolds number, $U_{inlet} = f\,(Re)$, over a range of 500 to 10,000. The height of the openings was fixed at 0.30 m, which represents a typical dimension for ventilation diffusers.

Boundary conditions were defined as follows: a low contaminant concentration C_C = 5 ppm was imposed on the vertical walls; the bottom wall was assigned a high concentration C_H = 25 ppm, while the top wall was considered adiabatic and impermeable. The cavity dimensions were set to 4 m in length and 3 m in height. The bottom wall is treated as a boundary condition with a high pollutant concentration; this condition can represent different real-world scenarios, such as a line of vehicles emitting *CO*.

After identifying the most efficient geometric configuration for contaminant removal, a hypothetical scenario corresponding to a localized fire was proposed. This case was analyzed at three different positions: near the air inlet, at the center of the cavity, and close to the outlet. In all scenarios, the contaminant source

was located at a constant height of 0.75 m, with a concentration of $C = C_H$. Assuming that emissions from vehicle fires occur at approximately this high.

3 Turbulent Convective Mathematical Model

This section describes the mathematical model employed to represent the transient turbulent convective flow. The turbulence model adopted was the standard k–ε model, which is widely recognized for its robustness and ability to predict turbulent flows in ventilated cavities and similar engineering applications. The model is based on the fundamental principles of conservation of mass (1), momentum (2), and species conservation (3). Since a transient analysis is considered, the temporal evolution term is included in all governing equations. The fluid is modeled as Newtonian and incompressible, with constant thermophysical properties within the study range. Viscous dissipation is considered negligible, and the effects of thermal radiation are not included but the concentration buoyancy is included. Given the low contaminant concentration levels, it is assumed that these do not affect the mass diffusion coefficient. The no-slip condition ($u = 0$) is imposed on solid surfaces, and the previously described boundary conditions are applied. The properties of the air—*CO* mixture are assumed to remain constant, except in the buoyancy term in the momentum equation, where the Boussinesq approximation is adopted to represent density variations caused by concentration gradients.

Continuity equation:

$$\frac{\partial(\rho)}{\partial t} + \frac{\partial(\rho\overline{u_i})}{\partial x_i} = 0 \tag{1}$$

Momentum conservation equation:

$$\frac{\partial(\rho\overline{u_i})}{\partial t} + \frac{\partial\left(\rho\overline{u_i u_j}\right)}{\partial x_j} = -\frac{\partial\overline{P}}{\partial x_i} + \frac{\partial}{\partial x_j}\left[\mu\left(\frac{\partial\overline{u_i}}{\partial x_j} + \frac{\partial\overline{u_j}}{\partial x_i}\right) - \rho\overline{u_i' u_j'}\right] + \rho g_i \beta_c\left(\overline{C} - C_\infty\right) \tag{2}$$

Contaminant (or chemical species) conservation equation (*CO*):

$$\frac{\partial\left(\rho\overline{C}\right)}{\partial t} + \frac{\partial\left(\rho\overline{u_j C}\right)}{\partial x_j} = \frac{\partial}{\partial x_j}\left(\rho D_{AB}\frac{\partial\overline{C}}{\partial x_j} - \rho\overline{u_j' C'}\right) \tag{3}$$

The terms $\rho\overline{u_i' u_j'}$ and $\rho\overline{u_j' C'}$ in the conservation equations represent; the Reynolds stress tensor and the turbulent mass flux vector. The presence of these terms introduces additional unknowns into the averaged Navier–Stokes equations, resulting in a non-closed system; that is, there are more unknown variables than available equations. This phenomenon is known as the turbulence closure problem.

To address this issue, closure models are required to express the turbulent terms in terms of the mean flow quantities. This is commonly achieved through the turbulent viscosity hypothesis, which establishes an analogy between turbulent stresses and mean velocity gradients. Accordingly, the Reynolds stress tensor can be related to the mean velocity via an effective turbulent viscosity μ_t, as expressed by the following relation:

$$\rho\overline{u_i' u_j'} = -\mu_t\left[\frac{\partial\overline{u}_i}{\partial x_j} + \frac{\partial\overline{u_j}}{\partial x_i}\right] + \frac{2}{3}\rho\kappa\delta_{ij} \tag{4}$$

Similarly, the turbulent mass flux can be modeled analogously to Fick's law for molecular diffusion:

$$\rho\overline{u_j' C'} = -\frac{\mu_t}{Sc_t}\frac{\partial \overline{C}}{\partial x_i} \tag{5}$$

The term $Sc_t = \frac{\nu_t}{D_t}$ is known as the turbulent Schmidt number.

The last three equations presented above share the turbulent viscosity, which can be estimated using the empirical Kolmogorov–Prandtl relation, expressed as follows:

$$\mu_t = C_\mu \frac{\rho k^2}{\varepsilon} \tag{6}$$

where the equations for the turbulent kinetic energy (k) and the turbulent kinetic energy dissipation rate (ε) are:

$$\frac{\partial(\rho k)}{\partial t} + \frac{\partial(\rho \overline{u}_i k)}{\partial x_i} = \frac{\partial}{\partial x_i}\left[\left(\mu + \frac{\mu_t}{\sigma_\kappa}\right)\frac{\partial k}{\partial x_i}\right] + P_\kappa + G_\kappa - \rho\varepsilon \tag{7}$$

$$\frac{\partial(\rho \varepsilon)}{\partial t} + \frac{\partial(\rho \overline{u}_i \varepsilon)}{\partial x_i} = \frac{\partial}{\partial x_i}\left[\left(\mu + \frac{\mu_t}{\sigma_\varepsilon}\right)\frac{\partial \varepsilon}{\partial x_i}\right] + C_{\varepsilon 1}\left[P_\kappa + C_{\varepsilon_3} G_\kappa\right]\frac{\varepsilon}{k} - C_{\varepsilon 2}\frac{\rho\varepsilon^2}{k} \tag{8}$$

The production due to shear stress and the buoyancy production-destruction of turbulent kinetic energy are defined, respectively, as follows:

$$P_\kappa = -\rho \overline{u_i' u_j'}\frac{\partial \overline{u}_i}{\partial x_j} = \tau_{ij}\frac{\partial \overline{u_i}}{\partial x_j} \tag{9}$$

$$G_\kappa = -\beta_C \overline{\rho u_i' C'} g_i = -\frac{\mu_t}{Sc_t} g_i \beta_C \frac{\partial \overline{C}}{\partial y_i} \tag{10}$$

Henkes et al. (1992) [53] suggested using a first-class wall boundary condition for the turbulent kinetic energy dissipation rate ($\varepsilon = \infty$, a large value), known as the H turbulence model. The corresponding values are determined empirically to establish the wall boundary conditions for this model. P_k represents the shear production of turbulent kinetic energy, while G_k denotes the buoyant production or destruction of turbulent kinetic energy. The model constants are defined as follows: $C_{\varepsilon 1} = 1.44$, $C_{\varepsilon 2} = 1.92$, $C_{\varepsilon 3} = tanh\,|v/u|$, $C_\mu = 0.09$, $\sigma_k = 1.0$, $\sigma_\varepsilon = 1.3$.

Boundary Conditions

The mathematical boundary conditions are defined as follows:

- Velocity components on solid surfaces are zero, $u_x = u_y = 0$.
- Inlet velocity, $u_{inlet} = f(Re)$, outlet velocity, $\partial u_x/\partial n = 0$, $\partial u_y/\partial n = 0$, n is the normal vector in the flow direction.
- Inlet concentration, $C = C_{inlet}$, for outlet concentration, $\partial C/\partial n = 0$.
- C_H and C_C are constant in bottom and vertical walls.
- Upper wall is impermeable.
- Turbulent boundary conditions in the inlet $k = 1.5\left(0.04 u_{inlet}\right)^{2.0}$, $\varepsilon_{inlet} = \left(k_{inlet}\right)^{0.5} / \left(0.1 H_i\right)$.
- Outlet turbulent boundary conditions, $\left(\partial k/\partial n\right) = 0$ and $\left(\partial \varepsilon/\partial n\right) = 0$.

4 Effectiveness of Contaminant Distribution (ε_C)

The analysis of contaminant distribution effectiveness is essential for evaluating the performance of ventilation systems, as this parameter quantifies the efficiency of polluted air distribution within an enclosed space. In this study, the contaminant distribution effectiveness was assessed under two main scenarios:

- Normal ventilation condition: In this case, the objective is to maintain adequate indoor air quality (IAQ). A high distribution effectiveness indicates that the air–contaminant mixture is efficiently diluted, leading to a uniform reduction of contaminant concentration throughout the domain.
- Localized fire condition: Under this scenario, the rapid generation of contaminants (mainly CO and smoke) poses a significant safety risk. A low distribution effectiveness implies that the contaminant spreads toward occupied zones rather than being efficiently extracted through the outlet openings, thereby compromising occupant safety.

The contaminant distribution effectiveness index is determined following the methodology proposed by [54], expressed as:

$$\varepsilon_C = \frac{C_{outlet} - C_{inlet}}{C_{average} - C_{inlet}} \tag{11}$$

where:

- C_{inlet} is the average contaminant concentration at the air inlet,
- $C_{average}$ is the average contaminant concentration within the cavity, and
- C_{outlet} is the average contaminant concentration at the outlet.

This parameter quantifies the efficiency with which the ventilation system removes the contaminant from the enclosure, where $\varepsilon_C > 1$ indicates effective extraction, and values below 1 reflect contaminant accumulation within the space.

5 Numerical Methodology

The system of equations describing the mathematical model is derived from the fundamental conservation principles of mass, momentum, energy, and chemical species diffusion. Due to the high level of nonlinearity and coupling among these equations, obtaining an analytical solution is not feasible. Therefore, the finite volume method (FVM) is employed for spatial discretization. The finite volume approach, introduced by Patankar [55], transforms the differential conservation equations into their integral form, which is solved over a computational mesh. In this mesh, scalar variables (such as temperature or concentration) are computed at the centers of the control volumes, while vector variables (such as velocity components) are estimated at the cell faces using appropriate interpolation or upwind schemes. This method is widely adopted because it enforces the conservation laws within each control volume, ensuring both numerical stability and global continuity of the solution. The SIMPLEC algorithm is used to couple the continuity and momentum equations, a standard approach in turbulent flow simulations. The resulting system of algebraic equations is solved using the Line-by-Line (LBL) method combined with the Alternating Direction Implicit (ADI) scheme, both of which are recognized for their stability and computational efficiency. To guarantee convergence, suitable relaxation factors are applied, and the iterative process is considered converged when the residuals of all governing equations fall below 1.0×10^{-8}. According to Xamán et al. [56], the general numerical procedure using the finite volume method can be summarized as follows:

1. The computational domain is divided into a finite number of control volumes, and initial values are assigned to all flow variables *(u, v, P*, and *C*).

2. The conservation equations for mass, momentum, and chemical species are integrated over each control volume and converted into algebraic form.
3. The fluxes of transported quantities across the cell faces are computed using appropriate interpolation schemes.

The resulting set of algebraic equations is then solved iteratively using pressure–velocity coupling algorithms such as SIMPLE or SIMPLEC until convergence of all flow variables is achieved.

5.1 Validation and Verification of the Numerical Code

To validate the developed numerical code, the obtained results were compared with the experimental data reported by Nielsen (1990) [57]. The reference case corresponds to an isothermal ventilated cavity under turbulent flow conditions, as illustrated in Fig. 2.

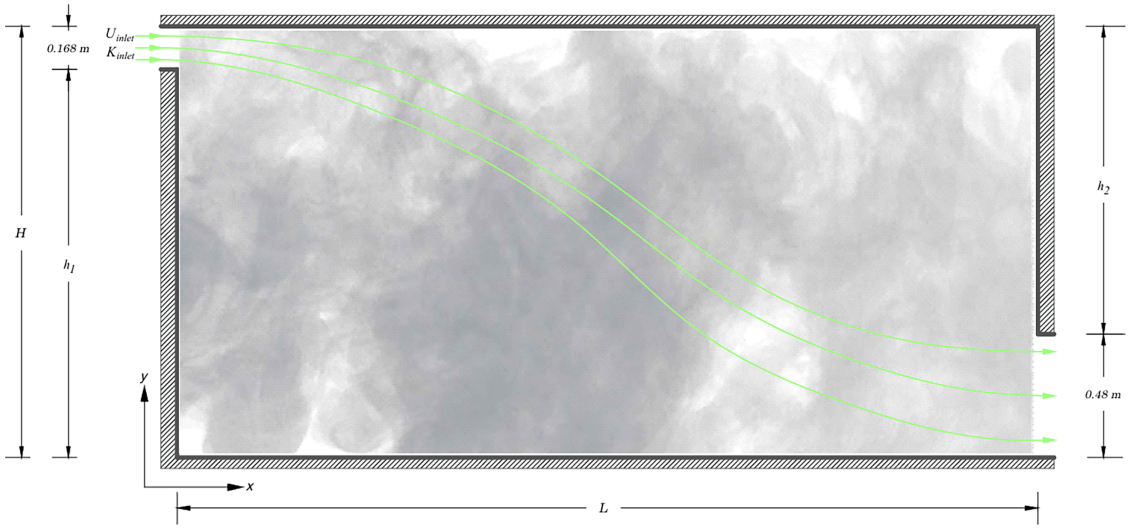

Figure 2: Isothermal ventilated cavity. [Nielsen, 1990] [57].

The model geometry is two-dimensional and consists of a rectangular cavity with a height of 3.0 m (H) and a length of 9.0 m (L). The inlet opening has a length of 0.168 m (APER1), while the outlet opening measures 0.48 m (APER2).

The flow was modeled using the standard k–ε turbulence model, considering the following thermophysical properties of air: $Re = 5 \times 10^3$, $\rho = 1.2064$ kg/m^3, $\mu = 1.5054 \times 10^{-5}$ kg/m·s, $\lambda = 2.569 \times 10^{-2}$ W/m·K, and $Cp = 1006$ J/kg·K, corresponding to a temperature of 20°C.

The dimensionless velocity profiles, U^*, are presented along four sections of the cavity (Fig. 3):

- In the first two sections, U^* is plotted along the Y^* axis for fixed positions $X^* = 1.0$ and $X^* = 2.0$, corresponding to regions near the inlet and outlet, respectively.
- In the remaining two sections, U^* is plotted along the X^* axis for fixed values of $Y^* = 0.028$ (near the floor) and $Y^* = 0.972$ (near the ceiling).

The comparison between the numerical and experimental results showed good agreement, validating the implementation of the finite volume method, the SIMPLEC coupling algorithm, and the k–ε turbulence model employed in the present study.

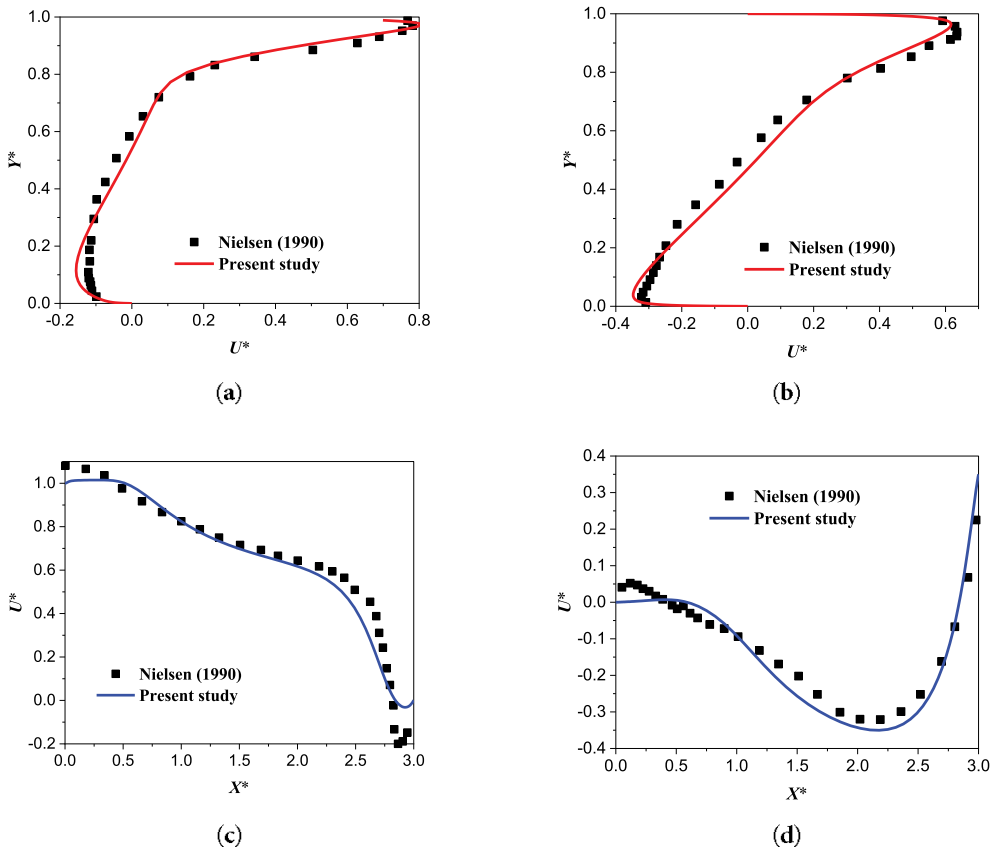

Figure 3: Dimensionless velocity (U^*) at different positions within the ventilated cavity. (**a**) x/H = 1.0; (**b**) x/H = 2.0; (**c**) y/H = 0.972; (**d**) y/H = 0.028 [57].

Fig. 3 shows the similarity between the numerical and experimental results, revealing a good overall agreement. A quantitative comparison indicates a maximum percentage deviation of 16.4% for the velocity component U^* at y/H = 0.972. This deviation was the largest observed and occurred at a point near the wall, where most turbulence models have difficulty accurately modeling the flow behavior.

A second comparison was carried out using the results reported by Lage et al. (1992) [58], who analyzed a rectangular ventilated cavity with different configurations and locations of internal contaminant sources. That study was conducted under both laminar and turbulent regimes; in the present work, the top–top (TT) configuration was used for comparison, yielding a maximum percentage difference of 1.4% in the average contaminant concentration for Case C (see Table 1).

Table 1: Comparison of the average concentration inside the cavity.

Source Location	Lage et al. 1992 [58]	Present Study	Difference %
Case A	75.26	74.6	0.87
Case B	55.51	56.2	1.22
Case C	47.91	47.2	**1.4**
Case D	122.24	121.8	0.3
Case E	73.16	73.2	0.05

The cavity dimensions were 2 m in length and 1 m in height, with inlet and outlet openings of 0.1 m each. Inside the cavity, a point source of contaminant was positioned in five different locations (Fig. 4), corresponding to the four corners (at one-sixth of the cavity's length and height) and the center.

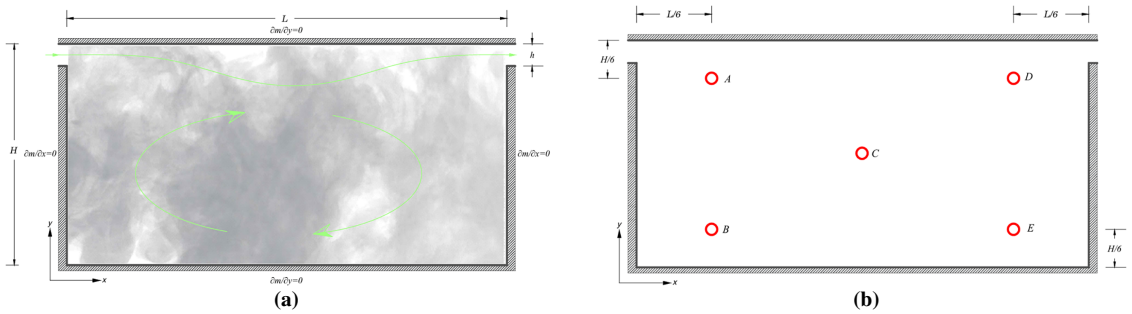

Figure 4: (**a**) Ventilated cavity under turbulent flow regime, (**b**) Locations of the contaminant source.

The study conducted by Lage et al. [58] assumed a Schmidt number Sc = 1, and verified that the values of kinematic viscosity and mass diffusion coefficient were numerically identical for the oxygen–carbon dioxide (O_2–CO_2) mixture. The corresponding thermophysical properties were calculated based on the gas composition.

The Reynolds number for the study was Re = 3000, corresponding to turbulent flow conditions. The problem was solved using a computational mesh of 81 × 61 control volumes, as reported by Lage et al. [58] (see Fig. 4).

Table 1 presents the average concentration values for each position of the contaminant source. It can be observed that the maximum deviation between the numerical and reference values was 1.4% at position C. Overall, the developed code demonstrates a good predictive capability and is considered suitable for solving this type of problem.

Once the verification and validation of the implemented code were completed and the reliability of the results was confirmed, the proposed case study of this thesis was solved. However, prior to that, a mesh independence study was conducted to ensure that the results were not influenced by numerical errors associated with the element size. This analysis is presented in the following section.

5.2 Numerical Mesh Analysis

In the numerical solution of engineering problems, it is essential to perform a mesh independence study to determine whether the results depend on the discretization size of the computational domain. This procedure involves evaluating the behavior of the variables of interest as the mesh is refined—that is, as the distance between nodes decreases.

It was observed that as the element size is progressively reduced, the variable values change until reaching a point where these variations become negligible. This point is considered the optimal mesh size, and its determination ensures that the results are independent of spatial discretization, depending on the physical conditions of the problem. For the present study, six initial mesh configurations were proposed with the following nodal distributions: 71 × 61, 81 × 71, 91 × 81, 101 × 91, 111 × 101, and 121 × 111. The results showed that the **111 × 101** mesh yielded a percentage difference of less than 0.5% compared to the finest mesh; therefore, it was selected as the optimal mesh. The comparative results are presented in Table 2.

Table 2: Effect of mesh refinement on velocity.

Mesh	Umax	%	Vmax	%
71 × 61	0.32	5.8	1.88	12.5
81 × 71	0.34	2.8	2.15	6.5
91 × 81	0.35	2.7	2.30	2.1
101 × 91	0.36	2.6	2.35	1.2
111 × 101	**0.37**	**0.2**	**2.38**	**0.4**
121 × 111	0.375	–	2.39	–

During the transient analysis, the numerical stability of the temporal scheme was evaluated. It was observed that for time steps greater than 1 s, iterative calculation tends to diverge, generating larger deviations with each iteration; thus, a value of $\Delta t = 0.1$ s was adopted, ensuring numerical stability and the correct temporal evolution of the variables.

All cases were simulated up to a total time of 450 s, corresponding to the lowest Reynolds number of $Re = 500$.

6 Discussion of Results

This section presents and analyzes the results obtained from the two-dimensional numerical study of turbulent convective flow with carbon monoxide (*CO*) transport inside a ventilated cavity. The analysis was carried out under transient conditions for four values of the Reynolds number: $Re = 500$, $Re = 1000$, $Re = 5000$, and $Re = 10{,}000$, considering three different geometric configurations, referred to as Case A, Case B, and Case C. In all cases, the airflow with a low concentration of carbon monoxide (1 ppm) enters through the lower part of the right wall. The outlet opening positions were as follows: Case A: upper part of the left wall, Case B: center of the left wall, Case C: lower part of the left wall.

The objective was to analyze the temporal evolution of contaminant concentration as a function of the Reynolds number and outlet configuration. The process starts with the initial condition at t = 0 s, and the variables were recorded at one-second intervals.

6.1 Case A: Upper-Left Outlet

For Case A scenario, shown in Fig. 5 with $Re = 5000$, it takes approximately 15 s to clear the *CO*—contaminated zone. At this moment, the lowest concentrations (8–9 ppm) are located in a thin layer near the bottom of the cavity. At t = 2 s, the airflow impacts the left wall, initiating the formation of recirculation zones. By t = 3 s, these recirculations extend toward the center of the cavity, and at t = 4 s, a large recirculation cell becomes established in the lower region. At t = 5 s, this circulation strengthens and expands upward. By t = 6 s, the recirculation extends to the right wall, causing the formation of a secondary vortex at the center of the cavity by t = 7 s. At t = 8 s, the lower airflow begins to displace the upper contaminated layer, introducing clean air into the domain. By t = 9 s, this clean air region widens, generating a sweeping effect that pushes the more polluted flow upward. Between t = 10 and 11 s, the air with lower *CO* concentration occupies nearly the lower half of the cavity. At t = 12 s, about three-quarters of the domain are cleared due to the incoming airflow. Finally, at t = 13–14 s, only a thin contaminated layer remains near the upper region, and by t = 15 s, the cavity reaches almost the minimum *CO* concentration (≈2 ppm) throughout the entire study area.

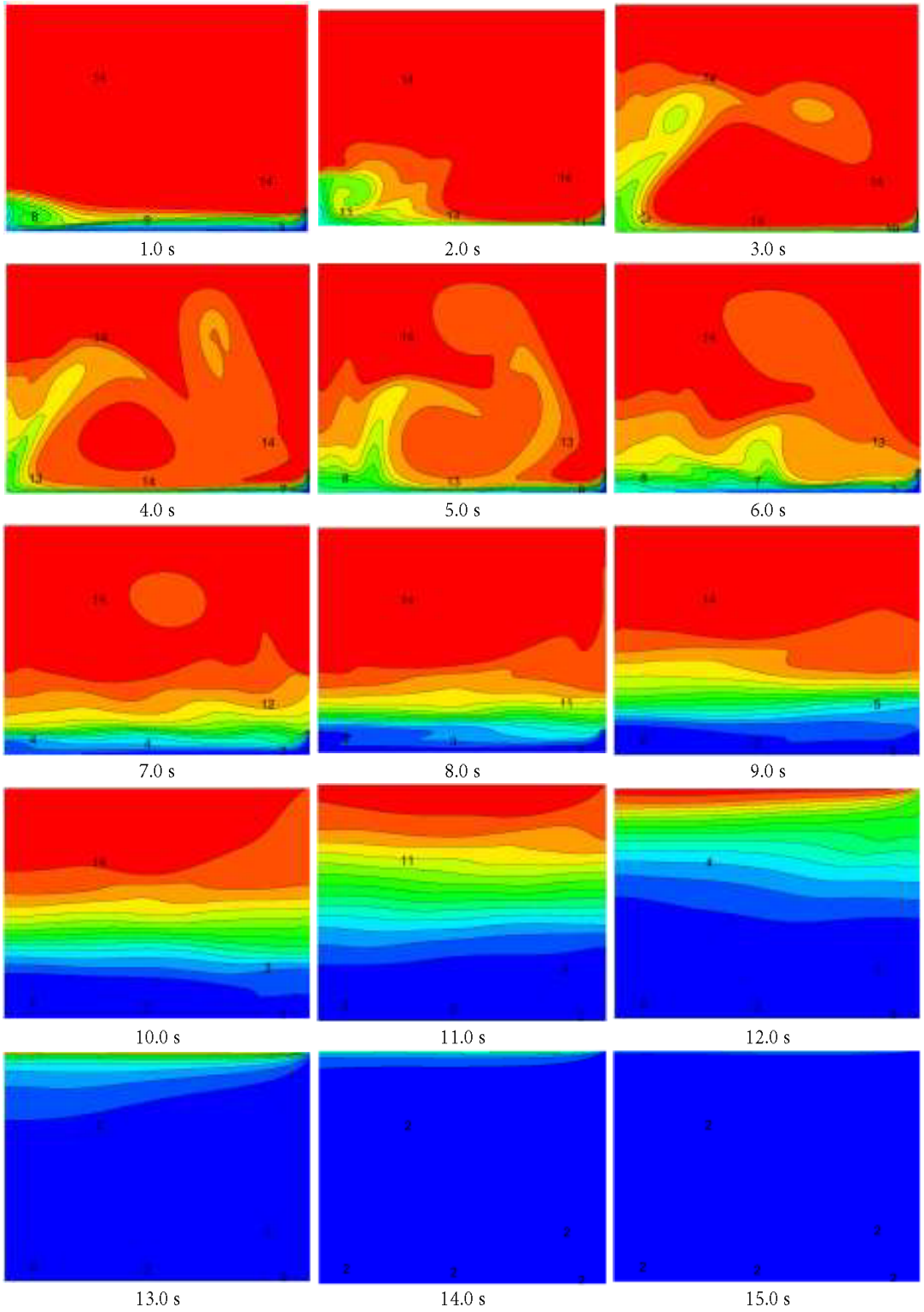

Figure 5: Temporal evolution of the *CO*-laden airflow inside the cavity from 1 to 15 s, for Case A with Re = 5000.

This same analysis was carried out for each Reynolds number considered and for all outlet configurations in the study.

At the beginning (t = 1 s), the maximum *CO* concentration inside the cavity reached 14 ppm, while the inlet air contained only 1 ppm, representing clean outdoor air. As time progresses, internal recirculation zones appear—first near the left wall, and later extending toward the center of the cavity. At t = 5 s, the main recirculation intensifies and expands upward; by t = 7 s, a secondary vortex forms in the central region. Between t = 9 and 10 s, the clean airflow entering from the inlet begins to sweep the contaminated zone from the bottom, displacing the *CO*-laden air toward the upper outlet. Finally, at t = 15 s, the average concentration inside the cavity returns to 1 ppm, equivalent to the clean inlet air. These results confirm that as the Reynolds number increases, the ventilation efficiency improves, and the purge time decreases significantly. Representative values for Case A are shown in Table 3, which includes only the time instants of interest—those corresponding to the steady-state condition. The data correspond to Re = 500, 1000, 5000 and 10,000. In all cases, the final average concentration matched that of the inlet air, achieving a complete and uniform cleaning of the cavity. For Re = 500, the required time extended up to 450 s due to low inlet velocities; for Re = 1000, it was 375 s; for Re = 5000, 15 s; and for Re = 10,000, only 11 s, clearly showing the influence of flow velocity on ventilation efficiency.

Table 3: Average contaminant concentration values inside the cavity for Case A between 1 and 450 s.

CASE A				
	Average concentration (ppm)			
Time (s)	***Re* = 500**	***Re* = 1000**	***Re* = 5000**	***Re* = 10,000**
1	14.96	14.96	14.33	13.70
5	14.90	14.86	13.45	11.80
10	14.83	14.72	9.45	1.40
11	14.82	14.68	7.10	1.0
12	14.81	14.64	4.04	1.0
13	14.79	14.60	1.81	1.0
14	14.78	14.56	1.24	1.0
15	14.77	14.53	1.0	1.0
375	1.5	1.0	1.0	1.0
450	1.0	1.0	1.0	1.0

6.2 Case B: Central Left Outlet

In Case B, the outlet is located at the center of the left wall, which modifies the flow patterns and the recirculation zones within the cavity. The times required to reach an average concentration of 1 ppm were: Re = 500: 195 s, Re = 1000: 88 s, Re = 5000: 16 s, and Re = 10,000: 12 s.

Table 4 presents the average *CO* concentration results inside the cavity for this configuration. Compared with Case A, a significant reduction in purge times is observed, attributed to the central location of the outlet, which facilitates the upward displacement of the contaminant from the lower regions toward the opening, thereby reducing the average path length before being expelled.

This configuration promotes a progressive bottom-to-top cleaning pattern, enhancing both the ventilation efficiency and the removal rate of contaminants.

Table 4: Average contaminant concentration values inside the cavity for Case B between 1 and 195 s.

CASE B				
	Average Concentration (ppm)			
Time (s)	***Re* = 500**	***Re* = 1000**	***Re* = 5000**	***Re* = 10,000**
1	14.93	14.86	14.32	13.69
5	14.85	14.70	13.48	11.81
10	14.68	14.33	9.49	1.31
11	14.61	14.19	7.27	1.14
12	14.54	14.04	4.0	1.0
13	14.46	13.88	1.92	1.0
14	14.39	13.71	1.23	1.0
15	14.32	13.53	1.11	1.0
16	14.24	13.34	1.0	1.0
88	3.17	1.0	1.0	1.0
195	1.0	1.0	1.0	1.0

6.3 Case C: Lower Left Outlet (Cross Ventilation)

Case C corresponds to the cross-ventilation configuration, where the outlet is located at the lower left side of the cavity, at the same height as the inlet. This arrangement proved to be the most efficient, with cleaning times of: Re = 500:191 s, Re = 1000: 87 s, Re = 5000: 15 s, and Re = 10,000: 11 s. Table 5 presents the average CO concentration values inside the cavity for this case study. The alignment in height between the inlet and the outlet creates a direct flow path, enabling the contaminant to be expelled efficiently without the need for strong recirculations. This type of ventilation is particularly effective in scenarios requiring rapid gas extraction, such as fires or localized leaks. Compared to the other configurations, Case C exhibited the shortest cleaning times, demonstrating greater effectiveness in air renewal and CO removal. For this reason, cross ventilation is considered highly efficient for quickly purging contaminated zones.

Table 5: Average contaminant concentration values inside the cavity for Case C between 1 and 195 s.

CASE C				
	Average concentration (ppm)			
Time (s)	***Re* = 500**	***Re* = 1000**	***Re* = 5000**	***Re* = 10,000**
1	14.93	14.86	14.31	13.86
5	14.85	14.70	13.50	11.91
10	14.68	14.33	9.48	1.20
11	14.61	14.19	7.23	1.0
12	14.53	14.03	4.04	1.0
13	14.46	13.88	1.92	1.0
14	14.39	13.69	1.21	1.0
15	14.31	13.52	1.0	1.0
16	14.23	13.31	1.0	1.0
87	1.76	1.0	1.0	1.0
191	1.0	1.0	1.0	1.0

It can be stated that, among the three analyzed cases (A, B, and C), Case C proved to be the most effective in reducing the time required to clear the contaminant zone. As can be seen in Table 6.

Table 6: Average contaminant concentration values (ppm) inside the cavity for all Cases.

***Re* = 10,000**			
Time (s)	**Case A**	**Case B**	**Case C**
1	13.70	13.69	13.86
5	11.80	11.81	11.91
10	1.40	1.31	1.2
11	1.0	1.14	1.0
12	1.0	1.0	1.0

This finding is particularly relevant in critical situations, such as indoor fire events, where the main objective is not to disperse the contaminant but to expel it as rapidly as possible through the outlet. Similarly, when the goal is to maintain indoor spaces free from contaminants—such as rest areas, offices, or common spaces—it is essential to ensure minimal concentrations of harmful substances. The ASHRAE Standard establishes a minimum number of air changes per hour (ACH) to maintain healthy and safe indoor conditions.

6.4 Air Changes Per Hour

The number of air changes per hour (ACH) was calculated for each configuration and Reynolds number, following the recommendations of the ASHRAE Standard. Table 7 presents the ACH values corresponding to study cases A, B, and C. As expected, Case C exhibited the highest ACH, reaching 47 air changes per hour.

It is important to note that the number of air changes primarily depends on the mass flow rate of air at the inlet and outlet, rather than on the specific location of the openings—provided they have the same dimensions and number. Therefore, for a given Reynolds number, all cases present the same ACH, although the flow distribution and the efficiency of contaminant removal vary according to the configuration.

In general, the results confirm that:

- The ventilation efficiency increases with the Reynolds number.
- Configurations with a lower outlet (cross ventilation) are more effective for contaminant removal.
- In low-velocity flows ($Re < 1000$), the transport process is dominated by natural convection, whereas at higher Reynolds numbers, forced convection becomes predominant.

The *CO* removal trend accelerates as the flow inertia increases, thereby reducing the contaminant residence time.

These results validate the physical behavior of the ventilated system and provide a solid basis for optimizing the design of ventilation systems in confined spaces.

6.5 Efficiency in Contaminant Distribution

The following section presents the analysis of the contaminant (*CO*) distribution efficiency. While the previous section evaluated the time required to reduce *CO* concentration, this one examines how uniformly it disperses within the cavity. This analysis is particularly relevant when the objective is to ensure that the contaminant spreads throughout most of the domain, avoiding localized accumulation zones and high concentration regions, which are undesirable from both air quality and safety perspectives.

Table 7: Air changes per hour (ACH) inside the cavity.

Re	**Case A**
500	2.3
1000	4.7
5000	23.5
10,000	47
Re	**Case B**
500	2.3
1000	4.7
5000	23.5
10,000	47
Re	**Case C**
500	2.3
1000	4.7
5000	23.5
10,000	47

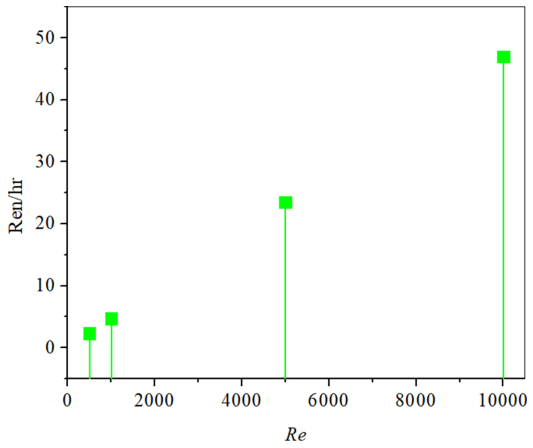

Table 8 presents the *CO* distribution efficiency values (ε_C) for Case A, showing the maximum values reached over time for each Reynolds number. A direct relationship is observed between the average concentrations and flow velocity, as both parameters depend on the inlet flow velocity. As *Re* increases, the time required to reach the maximum efficiency decreases; however, the time needed to achieve the peak efficiency is similar for $Re = 5000$ and $Re = 10,000$. The highest efficiency recorded corresponds to $Re = 5000$, with a value of $\boldsymbol{\varepsilon_C} = 14.364$. On the right-hand side of Table 8, the ε_C values over time for the different Reynolds numbers are presented, along with a graph showing the temporal evolution of the distribution for the four *Re* values. The zoomed-in view of the figure shows the values for time up to 20 s. The shorter time intervals correspond to higher Reynolds numbers ($Re = 5000$ and $Re = 10,000$), indicating that uniform dispersion is achieved more rapidly under higher flow velocities.

Table 9 presents the contaminant distribution efficiency ($\boldsymbol{\varepsilon_C}$) for Case B. As can be observed, the configuration with the outlet opening located at the center of the left wall does not promote a uniform dispersion of the contaminant. The values in the left column of the table show that, for all Reynolds numbers considered, the distribution efficiency decreases compared to Case A. In this case, the highest efficiency was achieved for $Re = 500$, corresponding to the lowest inlet velocity, with a value of $\boldsymbol{\varepsilon_C} = 2.038$, which remains relatively low. For higher Reynolds numbers, the efficiency is almost negligible; for example, at $Re = 10,000$, $\boldsymbol{\varepsilon_C}$ reaches only 0.055. The right column of Table 9 graphically displays the ε_C results over the time interval from 1 to 200 s. Since the values for $Re = 5000$ and $Re = 10,000$ reach their maximum within relatively short periods, a zoomed-in representation is recommended to better visualize their temporal evolution.

Table 10 presents the temporal values of contaminant distribution efficiency ($\boldsymbol{\varepsilon_C}$) for Case C under different Reynolds numbers. It is observed that $\boldsymbol{\varepsilon_C}$ decreases even further compared to Cases A and B, reaching its maximum value at $Re = 1000$ with $\boldsymbol{\varepsilon_C} = 0.326$, while the remaining values are nearly zero. This behavior is attributed to the cross-ventilation configuration, which limits the dispersion of the contaminant within the cavity. This characteristic has two practical implications. If the objective is to improve thermal comfort by introducing fresh air with a certain level of humidity, a configuration that enhances distribution efficiency is desirable. Conversely, in fire scenarios with high contaminant generation, a low $\boldsymbol{\varepsilon_C}$ value is preferred so that the flow can rapidly direct the gases toward the outlet. In this regard, cross-ventilation, as in

Case C, proves advantageous. The next section analyzes a scenario in which this configuration is particularly beneficial during a localized fire event.

Table 8: Distribution efficiency (ε_C) for Case A.

Time (s)	*Re* = 500	*Re* = 1000	*Re* = 5000	*Re* = 10,000
1	1.002	1.002	1.055	1.116
5	0.977	1.009	1.115	1.279
10	0.999	1.008	1.599	11.053
15	0.998	0.979	8.295	2.632
16	0.998	0.998	14.364	3.122
50	1.093	1.118	–	–
100	1.710	1.379	–	–
200	2.069	3.249	–	–
300	2.615	6.022	–	–
375	3.432	7.583	–	–
450	4.678	9.421	–	–

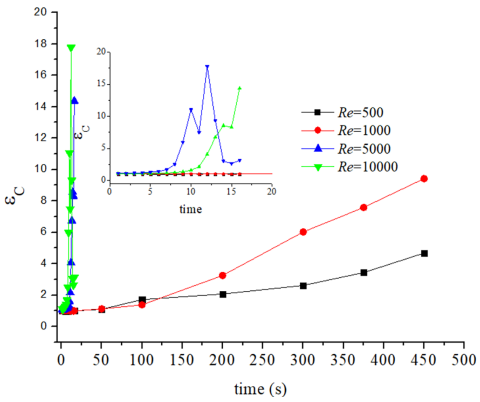

Table 9: Distribution efficiency (ε_C) CASE B.

Time (s)	*Re* = 500	*Re* = 1000	*Re* = 5000	*Re* = 10,000
1	1.002	1.010	1.055	1.116
5	0.977	0.982	1.079	1.185
10	0.999	0.982	1.330	0.002
15	0.998	1.058	0.059	0.082
88	2.490	0.233	0.265	0.036
195	2.038	0.175	0.332	0.055

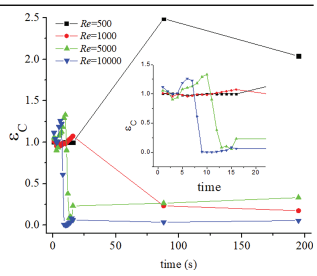

Table 10: Distribution efficiency (ε_C) CASE C.

Time (s)	*Re* = 500	*Re* = 1000	*Re* = 5000	*Re* = 10,000
1	1.005	1.010	0.336	0.236
5	0.952	0.913	0.848	0.005
10	0.989	0.973	0.042	0.005
15	0.881	0.523	0.018	0.040
16	0.871	0.554	0.043	0.058
87	0.002	0.007	0.019	0.008
191	0.0019	0.326	0.024	0.008

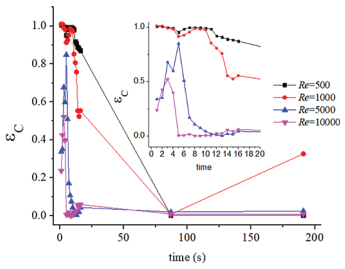

This behavior has relevant practical implications:

- In situations where the goal is to improve thermal comfort through the introduction of fresh air with a certain level of humidity, a ventilation configuration that increases distribution efficiency is desirable.

- Conversely, in the event of a fire or a localized emission of pollutants, a configuration with low distribution efficiency is more advantageous, as it facilitates the rapid evacuation of contaminated air.

The following section specifically analyzes a case in which cross-ventilation proves beneficial in the presence of a localized pollutant emission source.

6.6 Localized Fire Analysis

Fig. 6 illustrates the behavior of carbon monoxide (*CO*) flow generated by a localized fire, which produces high pollutant concentrations (ppm). Three possible locations of the fire source were analyzed: (1) near the left wall, where the outlet opening is located; (2) at the center of the cavity; and (3) near the air inlet. Fig. 6 corresponds to the scenario in which the fire is located close to the outlet, associated with Case C, which exhibited the most efficient cross-ventilation configuration. This arrangement does not promote internal dispersion of the contaminant but instead directs it rapidly toward the outlet, which is advantageous in preventing its propagation to other regions. At the initial second, the *CO* concentration rises rapidly upward since the incoming airflow has not yet reached that region. At 5 s, the main flow reaches the lower part of the left wall and is redirected toward the opposite side of the cavity, displacing the contaminant in the direction opposite to the inlet flow. At 10 s, the air entering the cavity fills the lower region, reducing the upward intensity of the contaminant. By 15 s, most of the cavity is occupied by clean air, leaving only a narrow band of *CO* concentration in the upper zone. Between 20 and 25 s, the concentration in the upper region decreases and then intensifies again until it completely occupies that area. At 30 s, the upper zone exhibits a uniformly low concentration, indicating that most of the *CO* has been expelled. The intensity of the contaminated flow decreases significantly due to air renewal. By 35 s, the incoming airflow drives the contaminant toward the outlet, and finally, at 40 s, the *CO* is fully directed toward the opening, reducing its concentration, although it does not reach the minimum level of 1 ppm since the fire source continues to generate pollutants.

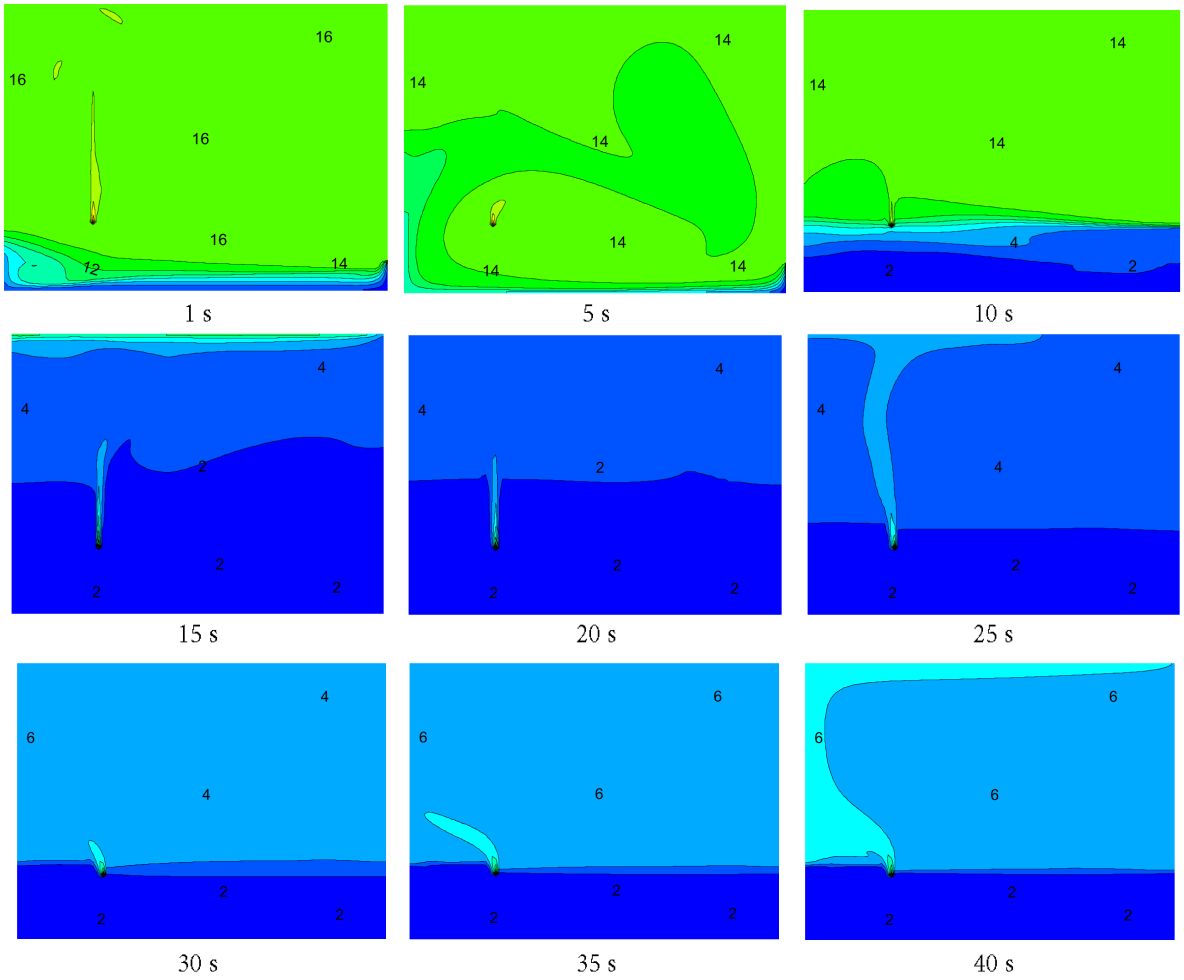

Figure 6: Behavior of the contaminant flow considering the concentration generated by a localized fire near the outlet opening for Case C.

When comparing the three study cases (A, B, and C), the behavior of the contaminant flow is observed when the source is located near the outlet opening, as illustrated in Fig. 7.

Fig. 7 illustrates the behavior of the contaminant flow for the three study cases (A, B, and C), considering the source located near the outlet. Three-time instants are presented—1, 25, and 50 s—covering the interval in which the concentration reaches a quasi-steady state. At 1 s, all three cases exhibit a similar flow pattern. At 25 s, the differences become evident: in Case A, the contaminant reaches the upper region forming a thin flow line; in Case B, the flow tends to expand laterally; while in Case C, the contaminant occupies the left and upper zones of the cavity. At 50 s, when the steady state is reached, the lowest concentration is observed near the lower wall in all cases, whereas the highest concentration is found in Case B.

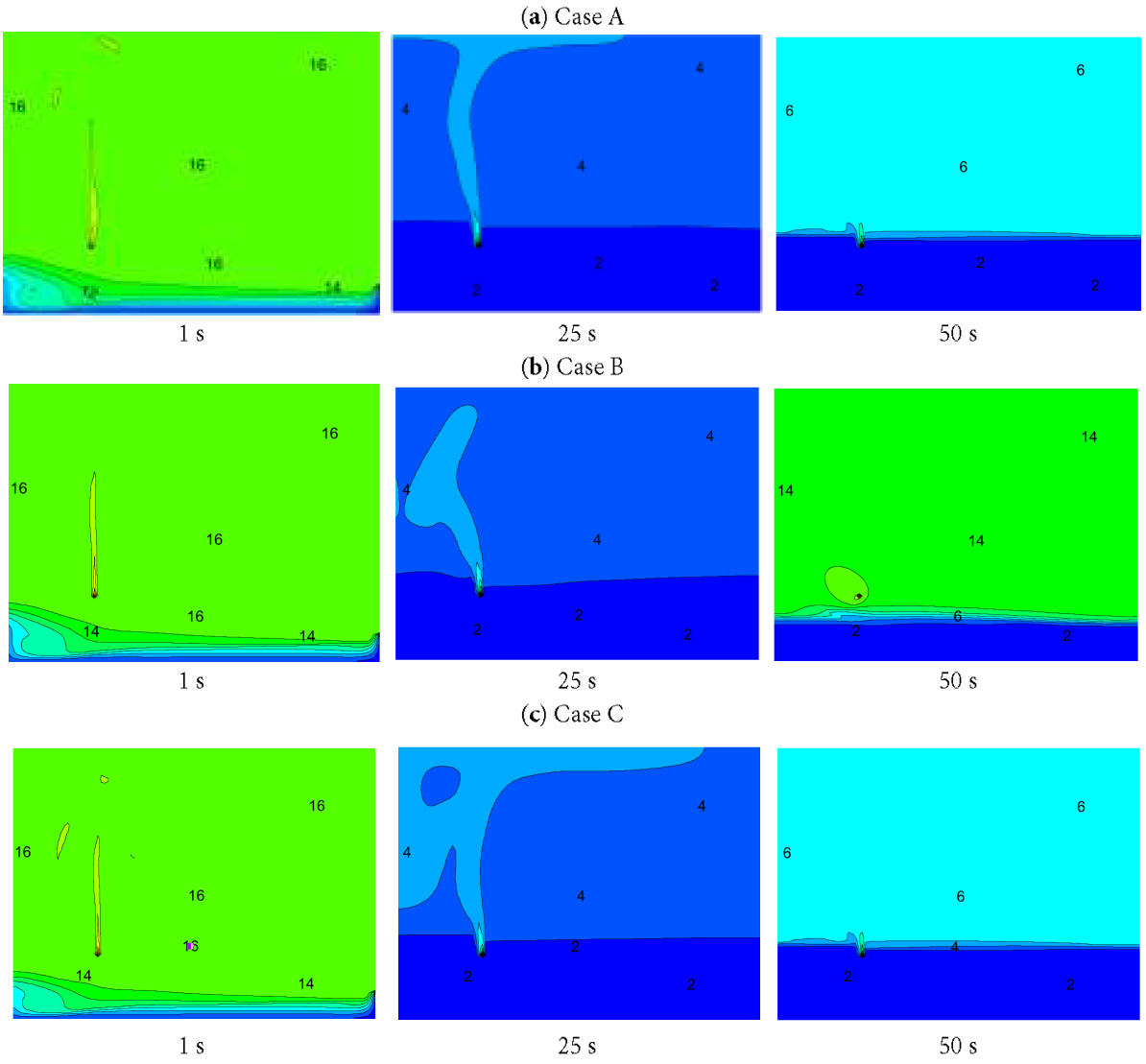

Figure 7: Representation of the contaminant (*CO*) flow inside the cavity for (**a**) Case A, (**b**) Case B, and (**c**) Case C, all corresponding to a Reynolds number of *Re* = 5000, when the contaminant source is located near the outlet opening.

Fig. 8 illustrates the contaminant flow pattern for the three studied cases (A, B, and C) at three-time instants: 1, 25, and 50 s, considering that the contaminant source (localized fire) is located at the center of the cavity. At 1 s, in (a) Case A, the concentration rises in a filament-like shape toward the upper wall. In (b) Case B, the momentum of the inlet flow prevents the contaminant from dispersing, whereas in (c) Case C, the concentration extends upward in a manner similar to Case A. At 25 s, the contaminant in Case A tends to move toward the left, in contrast to Case B, where it shifts to the right. These opposite directions are relevant when controlling the contaminant trajectory is desired. At 50 s, all cases have reached a steady state, exhibiting a very similar flow behavior and comparable concentration distributions.

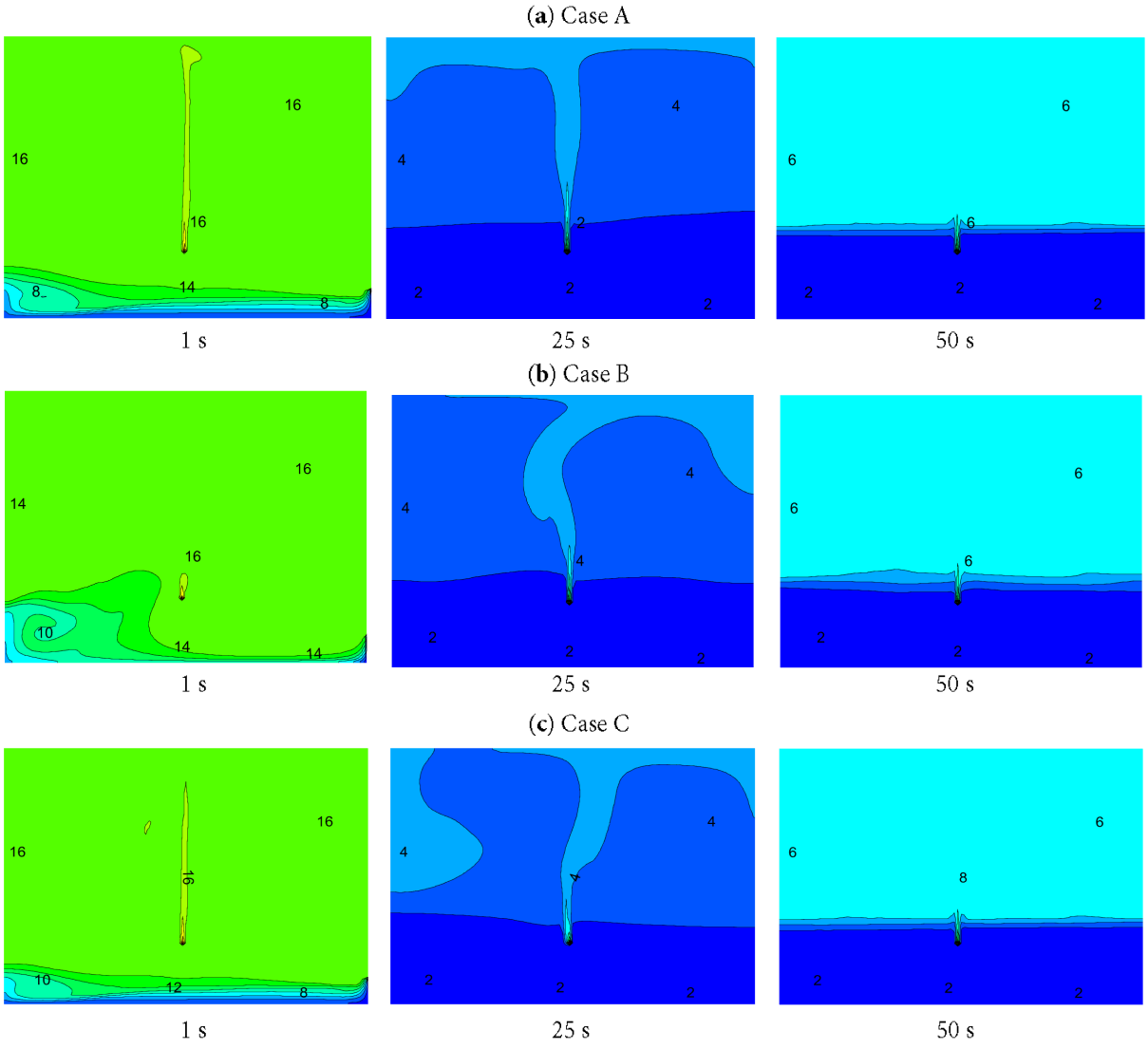

Figure 8: Representation of the contaminant (*CO*) flow inside the cavity for (**a**) Case A, (**b**) Case B, and (**c**) Case C, all at $Re = 5000$, when the contaminant source is located at the center of the cavity.

Fig. 9 shows the behavior of the contaminant flow when the source is located near the air inlet. At 1 s, the three cases exhibit a similar pattern; however, significant differences are observed at 25 s. Due to the proximity of the source to the inlet, the airflow promotes a rapid dispersion of the contaminant, effectively reducing its concentration, as seen in subfigures (a), (b), and (c). At 50 s, the highest concentration is recorded in Case B, while Cases A and C display a nearly similar behavior. Nevertheless, in Case C, the region of high concentration reaches a lower height compared to Case A, which is attributed to the position of the outlet opening.

6.7 Temporal Velocity Behavior

The velocity behavior of the flow is shown in Fig. 10, representing the velocities along the horizontal axis at the mid-height of the cavity.

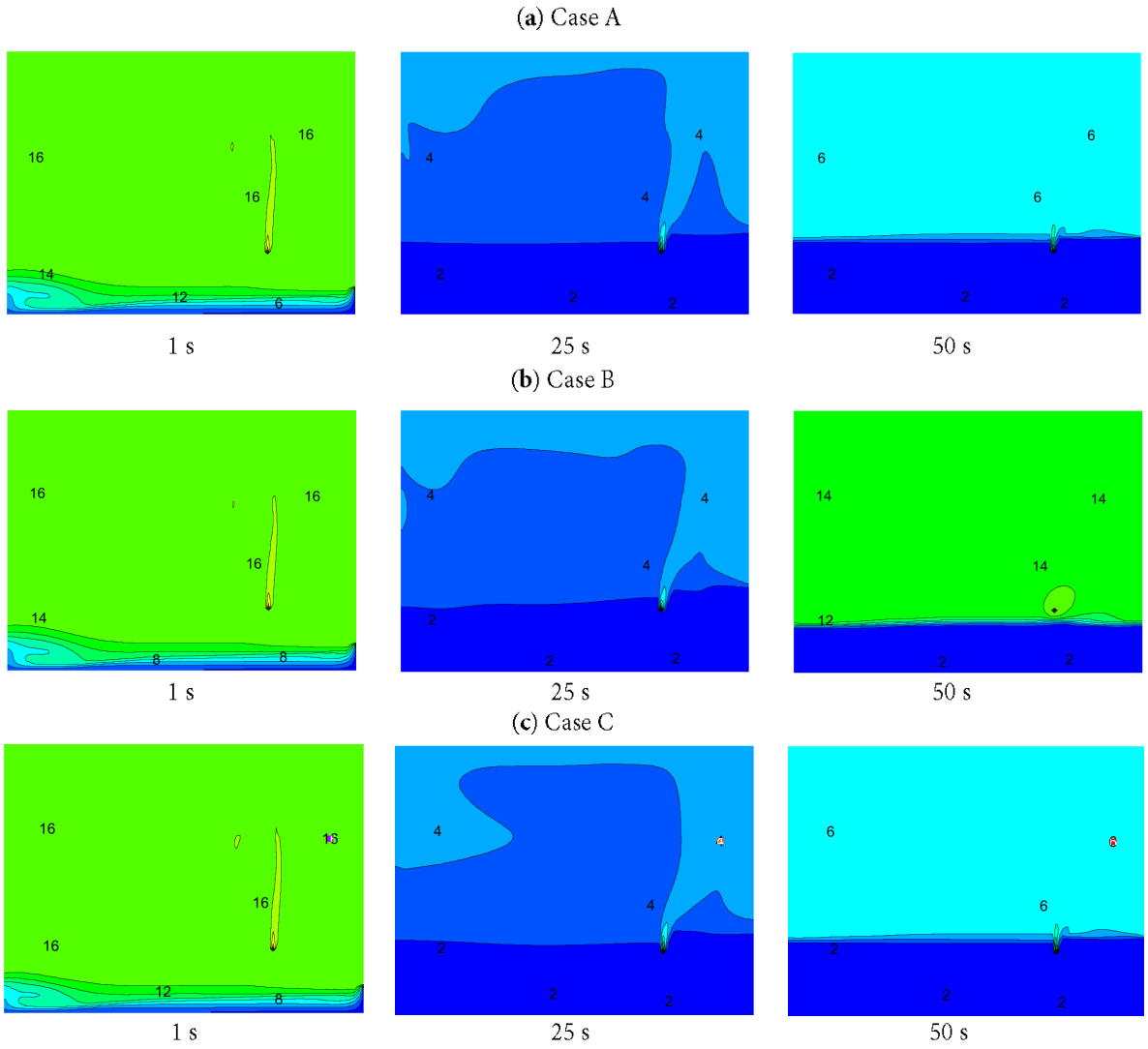

Figure 9: Representation of the contaminant (*CO*) flow inside the cavity for (**a**) Case A, (**b**) Case B, and (**c**) Case C, all corresponding to a Reynolds number of *Re* = 5000, when the contaminant source is located near the inlet.

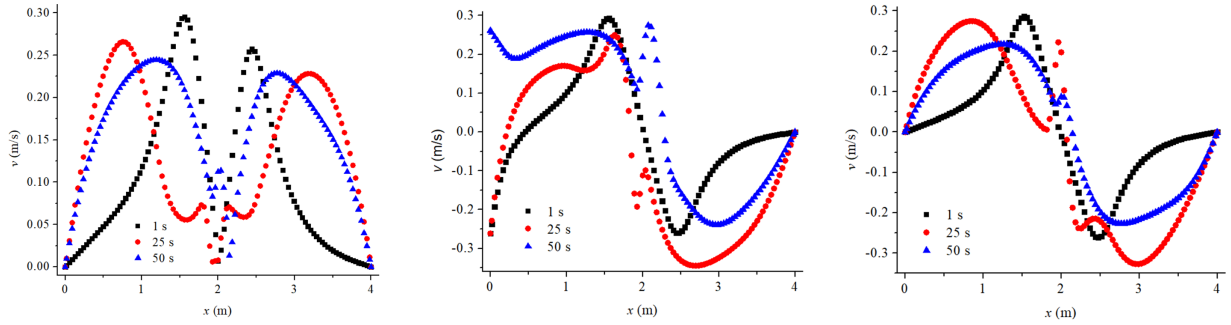

(**a**) Case A (**b**) Case B (**c**) Case C

Figure 10: Temporal velocity behavior for the case of the contaminant source located at the center of the cavity for (**a**) Case A, (**b**) Case B, and (**c**) Case C, considering *Re* = 5000.

The velocities are presented for three instants covering the interval in which the flow reaches a steady state for Re = 5000. In Case A (Fig. 10a), the velocities diverge due to the momentum imparted by the source located at the center of the cavity, at a height of 0.75 m from the base. It is important to note that, in this case, the outlet opening is located at the top of the left wall. For Cases B (Fig. 10b) and Case C (Fig. 10c), the velocity patterns tend to converge, with the most noticeable differences occurring only in the left region of the cavity, where the outlet is positioned. As time progresses, the velocity values stabilize, reaching an almost constant behavior after 50 s, indicating that the flow has attained a steady-state regime throughout the cavity.

7 Conclusions

It was found that the time required to reduce *CO* concentration within the cavity decreases significantly as *Re* increases. For all three study cases, cleaning times were shorter with higher inlet flow velocities. For instance, in Case A, the cleaning time ranged from 450 s for Re = 500 to only 11 s for Re = 10,000. The ventilation geometry has a significant impact on cleaning efficiency. Case C, with the outlet at the same height as the inlet (cross-ventilation), was the most effective in rapidly removing contaminants. Case B, with the outlet at mid-height, exhibited intermediate cleaning times, while Case A, with the outlet at the top, showed the longest times. Contaminant distribution efficiency ($\boldsymbol{\varepsilon_C}$) depends on both outlet location and *Re* number. In normal ventilation scenarios, high $\boldsymbol{\varepsilon_C}$ values indicate a more uniform distribution of the contaminant, which favors thermal comfort. However, in localized fire scenarios, low distribution efficiency is desirable because it directs contaminants quickly toward the outlet, preventing their dispersion throughout the cavity. Simulations showed that when the contaminant source is near the outlet, *CO* flow is efficiently directed outward, reducing exposure in the rest of the cavity. This behavior is ideal for safety applications in enclosed spaces, such as rooms, offices, or shared areas, where minimizing contaminant concentration quickly is critical.

Practical applications and recommendations

- For ventilation aimed at thermal comfort, it is advisable to maximize distribution efficiency ($\boldsymbol{\varepsilon_C}$) through appropriate placement of inlets and outlets.
- For safety scenarios (fires or localized contaminant release), cross-ventilation with the outlet at the same height as the inlet (Case C) provides the most rapid contaminant evacuation.
- These results can serve as a guideline for designing ventilation systems in confined spaces, balancing cleaning efficiency, contaminant distribution, and occupational safety.

Acknowledgement: We would like to extend our special thanks to SECIHTI (Secretariat of Science, Humanities, Technology, and Innovation) for awarding María Isabel Hernández López a grant to develop the research project related to this study.

Funding Statement: The authors received no specific funding for this study.

Author Contributions: The authors confirm contribution to the paper as follows: study conception and design: J. Serrano-Arellano, M. I. Hernández-López; data collection: E. V. Macias-Melo, F. N. Demesa-López, M. I. Hernández-López; analysis and interpretation of results: J. Serrano-Arellano, M. I. Hernández-López; draft manuscript preparation: M. I. Hernández-López, J. Serrano-Arellano. All authors reviewed and approved the final version of the manuscript.

Availability of Data and Materials: The data that support the findings of this study are available from the corresponding author, [J. Serrano-Arellano], upon reasonable request.

Ethics Approval: Not applicable.

Conflicts of Interest: The authors declare no conflicts of interest.

Nomenclature

C	Concentration of chemical species, Kg/m^3, ppm.
C_∞	Concentration of reference chemical species, Kg/m^3, ppm.
C_{inlet}	Concentration of chemical species at the mixture inlet, Kg/m^3, ppm.
C_{outlet}	Concentration of chemical species at the mixture outlet, Kg/m^3, ppm.
C_{source}	Contaminant source of the chemical species, Kg/m^3, ppm.
Cp	Specific heat of the air, J/Kg K.
$C_{\varepsilon 1}, C_{\varepsilon 2}, C_{\varepsilon 3}$	Constants of the turbulence model.
D_{AB}	Diffusion coefficients of the chemical specie from A to B, m^2/s.
g	Acceleration due to gravity, m/s^2.
h_{ext}	External convective heat transfer coefficient, W/m^{2}K.
H_i	Aperture height at the mixture inlet, m.
Hx	Cavity width, m.
Hy	Cavity height, m.
n	Normal direction.
P	Fluid pressure, N/m^2.
Pr	Prandtl number, $Pr = \upsilon/\alpha$.
Re	Reynolds number, $Re = (u_{inlet})(\rho)(H_i)/\mu$.
$S\varphi$	Source term.
u	Velocity in the horizontal direction, m/s.
u_{inlet}	Velocity in the horizontal direction at the inlet, m/s.
v	Velocity in the vertical direction, m/s.
x, y	Coordinate x or y.
Greeks	
α	Thermal diffusivity, m^2/s.
β_C	Coefficient of concentration expansion, $\beta_C = 1/C_{prom}$, (Kg/m^3)$^{-1}$.
Γ	Diffusion coefficient.
ε	Rate of dissipation of turbulent kinetic energy, m^2/s^3.
$\overline{\varepsilon}_C$	Overall effectiveness coefficient for contaminant distribution.
κ	Turbulent energy kinetic, m^2/s^2.
μ	Dynamic viscosity of the mixture (Aire-CO), kg/m s.
μ_t	Turbulent viscosity.
υ	Kinematic viscosity of the mixture (Air-CO), m^2/s.
ρ	Density of the mixture (Air-CO), kg/m^3.
σ	Stefan-Boltzman constant, 5.67×10^{-8}, W/m^2 K^4.
σ_t	Turbulent Prandtl number.
ϕ	Dependent general variable (u, v, P, C).

References

1. Ho JC, Xue H, Tay KL. A field study on determination of carbon monoxide level and thermal environment in an underground car park. Build Environ. 2004;39(1):67–75. doi:10.1016/j.buildenv.2003.07.006.
2. Bobylev N. Underground space as an Urban indicator: measuring use of subsurface. Tunn Undergr Space Technol. 2016;55:40–51. doi:10.1016/j.tust.2015.10.024.
3. Yang B, Yao H, Wang F. A review of ventilation and environmental control of underground spaces. Energies. 2022;15(2):409. doi:10.3390/en15020409.
4. Chu CR, Su ZY. Natural ventilation design for underground parking garages. Build Environ. 2023;227:109784. doi:10.1016/j.buildenv.2022.109784.
5. Tan CCL, Finney KN, Chen Q, Russell NV, Sharifi VN, Swithenbank J. Experimental investigation of indoor air pollutants in residential buildings. Indoor Built Environ. 2013;22(3):471–89. doi:10.1177/1420326x12441806.

6. Amirkhani Ardeh S, Khaloo SS, Gholamnia R, Abtahi M, Saeedi R. Assessment of indoor air pollutant concentrations and emissions from natural gas cooking burners in residential buildings in Tehran, Iran. Air Qual Atmos Health. 2020;13(4):409–20. doi:10.1007/s11869-020-00804-y.
7. Zhao Y, Song X, Zhao J. Assessment of PM1 number concentration with respect to traffic flow and thermal environment in a residential underground garage. Glob Nest J. 2018;20:304–15. doi:10.30955/gnj.002372.
8. World Health Organization (WHO). Las nuevas directrices mundiales de la OMS sobre la calidad del aire. 2021 [cited 2025 Feb 25]. Available from: https://www.who.int/es/news/item.
9. Environmental Protection Agency (EPA). Impacto del monóxido de carbono en la calidad del aire de los interiores. 2024 [cited 2025 Feb 25]. Available from: https://espanol.epa.gov/cai/impacto-del-monoxido-de-carbono-en-la-calidad-del-aire-de-los-interiores.
10. Chung KC, Hsu SP. Effect of ventilation pattern on room air and contaminant distribution. Build Environ. 2001;36(9):989–98. doi:10.1016/S0360-1323(00)00051-2.
11. Serrano-Arellano J, Gijón-Rivera M, Riesco-Ávila JM, Xamán J, Álvarez G. Numerical investigation of transient heat and mass transfer by natural convection in a ventilated cavity: outlet air gap located close to heat source. Int J Heat Mass Transf. 2014;76:268–78. doi:10.1016/j.ijheatmasstransfer.2014.04.055.
12. Chow WK, Wong LT, Fung WY. Field study on the indoor thermal environment and carbon monoxide levels in a large underground car park. Tunn Undergr Space Technol. 1996;11(3):333–43. doi:10.1016/0886-7798(96)00025-9.
13. Chow WK. Design of ventilation system in a big enclosed car park using computational fluid dynamics. Archit Sci Rev. 1996;39(3):141–5. doi:10.1080/00038628.1996.9696809.
14. Chan MY, Chow WK. Car park ventilation system: performance evaluation. Build Environ. 2004;39(6):635–43. doi:10.1016/j.buildenv.2003.10.009.
15. Špiljar Ž, Drakulić M, Schneider DR. Analysis of jet fan ventilation system installed in an underground car park with partition walls. J Sustain Dev Energy Water Environ Syst. 2018;6(2):228–39. doi:10.13044/j.sdewes.d5.0180.
16. Zhao R, Zhou L, Ma J. CFD design of ventilation system for large underground bus terminal in Macau Barrier Gate. J Wind Eng Ind Aerodyn. 2018;179:1–13. doi:10.1016/j.jweia.2018.05.010.
17. Mousavi MS, Ashrafi K, Motlagh MSP, Niksokhan MH, Vosoughifar HR. Experimental and numerical analysis of CO concentration dispersion of vehicular exhaust emissions in isolated environment. Environ Model Assess. 2017;22(5):431–44. doi:10.1007/s10666-016-9546-y.
18. Aminian J, Maerefat M, Heidarinejad G. The enhancement of pollutant removal in underground enclosed parking lots by reconsideration of the exhaust vent heights. Tunn Undergr Space Technol. 2018;77:305–13. doi:10.1016/j.tust.2018.04.005.
19. Peng SB. Carbon monoxide diffusion and ventilation in underground garage. Appl Ecol Env Res. 2019;17(4):9065–81. doi:10.15666/aeer/1704_90659081.
20. Yu J, Kang Y, Zhai Z. Advances in research for underground buildings: energy, thermal comfort and indoor air quality. Energy Build. 2020;215:109916. doi:10.1016/j.enbuild.2020.109916.
21. Faramarzi A, Lee J, Stephens B, Heidarinejad M. Assessing ventilation control strategies in underground parking garages. Build Simul. 2021;14(3):701–20. doi:10.1007/s12273-020-0677-3.
22. Li M, Aminossadati SM, Wu C. Numerical simulation of air ventilation in super-large underground developments. Tunn Undergr Space Technol. 2016;52:38–43. doi:10.1016/j.tust.2015.11.009.
23. Kong KH, Chong WT, Koh VL. Human behaviour-dependent and variable-flow-reversible mechanical ventilation system design in an underground parking facility. Indoor Built Environ. 2019;28(10):1324–40. doi:10.1177/1420326x19832955.
24. Mukhtar A, Yusoff MZ, Ng KC. The potential influence of building optimization and passive design strategies on natural ventilation systems in underground buildings: the state of the art. Tunn Undergr Space Technol. 2019;92:103065. doi:10.1016/j.tust.2019.103065.
25. Porras-Amores C, Mazarrón FR, Cañas I, Villoría Sáez P. Natural ventilation analysis in an underground construction: CFD simulation and experimental validation. Tunn Undergr Space Technol. 2019;90(7):162–73. doi:10.1016/j.tust.2019.04.023.

26. Cho J, Kim J, Park W, Kim Y. A step-by-step numerical method for optimization of mechanical ventilation in deep underground enclosed parking lots: a case-design study. J Build Eng. 2021;42:102799. doi:10.1016/j.jobe.2021.102799.
27. Xue H, Ho JC. Modelling of heat and carbon monoxide emitted from moving cars in an underground car park. Tunn Undergr Space Technol. 2000;15(1):101–15. doi:10.1016/S0886-7798(00)00035-3.
28. Krarti M, Ayari A. Ventilation for enclosed. ASHRAE J. 2001;43(2):52–7.
29. Papakonstantinou K, Chaloulakou A, Duci A, Vlachakis N, Markatos N. Air quality in an underground garage: computational and experimental investigation of ventilation effectiveness. Energy Build. 2003;35(9):933–40. doi:10.1016/S0378-7788(03)00020-3.
30. Sittisak P, Charinpanitkul T, Chalermsinsuwan B. Enhancement of carbon monoxide removal in an underground car park using ventilation system with single and twin jet fans. Tunn Undergr Space Technol. 2020;97:103226. doi:10.1016/j.tust.2019.103226.
31. Kmecová M, Krajčík M, Straková Z. Designing jet fan ventilation for an underground car park by CFD simulations. Period Polytech Mech Eng. 2018;63(1):39–43. doi:10.3311/ppme.12529.
32. Williams SV, Close R, Piel FB, Barratt B, Crabbe H. Characterising carbon monoxide household exposure and health impacts in high- and middle-income countries—a rapid literature review, 2010–2024. Int J Environ Res Public Health. 2025;22(1):110. doi:10.3390/ijerph22010110.
33. Awbi HB. Ventilation of buildings. 2nd ed. London, UK: Spon Press; 2003. doi:10.4324/9780203634479.
34. Chow WK. On safety systems for underground car parks. Tunn Undergr Space Technol. 1998;13(3):281–7. doi:10.1016/S0886-7798(98)00060-1.
35. Li YM, Hao Z. On the characteristics of fires in the underground buildings and the measures against them. J Chin People's Armed Police Force Acad. 2003;19(6):27–8. doi:10.4337/9781783473878.00017.
36. Chow WK. Simulation of tunnel fires using a zone model. Tunn Undergr Space Technol. 1996;11(2):221–36. doi:10.1016/0886-7798(96)00012-0.
37. Carvel RO, Beard AN, Jowitt PW, Drysdale DD. Variation of heat release rate with forced longitudinal ventilation for vehicle fires in tunnels. Fire Saf J. 2001;36(6):569–96. doi:10.1016/S0379-7112(01)00010-8.
38. Kurioka H, Oka Y, Satoh H, Sugawa O. Fire properties in near field of square fire source with longitudinal ventilation in tunnels. Fire Saf J. 2003;38(4):319–40. doi:10.1016/S0379-7112(02)00089-9.
39. Schleich JB, Cajot LG, Pierre M, Brasseur M. Development of design rules for steel structures subjected to natural fires in closed car parks. Luxembourg City, Luxembourg: European Commission; 1999.
40. Kitano T, Sugawa O, Masuda H, Ave T, Uesugi H. Large scale fire tests of 4-story type car park part 1: the behavior of structural frame exposed to the fire at the deepest part of the first floor. In: Fourth Asia-Oceania Symposium on Fire Science and Technology; 2000 May 24–26; Tokyo, Japan. p. 527–38.
41. McGrattan K, Forney G, Floyd J, Hostikka S, Prasad K. Fire dynamics simulator (version 3)—user's guide. Gaithersburg, MD, USA: National Institute of Standards and Technology; 2002. doi:10.6028/NIST.IR.6784e2002.
42. Santoso MA, Bey Z, Nugroho YS. CFD study on the ventilation system and shape configuration of underground car park in case of fire. Appl Mech Mater. 2015;758:143–51. doi:10.4028/www.scientific.net/amm.758.143.
43. Vauquelin O, Mégret O. Smoke extraction experiments in case of fire in a tunnel. Fire Saf J. 2002;37(5):525–33. doi:10.1016/S0379-7112(02)00014-0.
44. Zhang XG, Guo YC, Chan CK, Lin WY. Numerical simulations on fire spread and smoke movement in an underground car park. Build Environ. 2007;42(10):3466–75. doi:10.1016/j.buildenv.2006.11.002.
45. Yao Y, Xia Z, Wang R, Ren F, Gao Z, Zhao J, et al. Smoke movement and control in tunnels under construction: recent research progress and future directions. Fire. 2023;6(5):191. doi:10.3390/fire6050191.
46. Cavazzuti M, Tartarini P. Pool fires within a large under-ventilated environment: experimental analysis and numerical simulation using OpenFOAM. Fire Technol. 2024;60(3):1891–915. doi:10.1007/s10694-024-01554-4.
47. Merci B, Shipp M. Smoke and heat control for fires in large car parks: lessons learnt from research? Fire Saf J. 2013;57:3–10. doi:10.1016/j.firesaf.2012.05.001.
48. Tilley N, Deckers X, Merci B. CFD study of relation between ventilation velocity and smoke backlayering distance in large closed car parks. Fire Saf J. 2012;48:11–20. doi:10.1016/j.firesaf.2011.12.005.

49. Deckers X, Haga S, Tilley N, Merci B. Smoke control in case of fire in a large car park: CFD simulations of full-scale configurations. Fire Saf J. 2013;57(5):22–34. doi:10.1016/j.firesaf.2012.02.005.
50. Tony Enright PA. Impact of jet fan ventilation systems on sprinkler activation. Case Stud Fire Saf. 2014;1:1–7. doi:10.1016/j.csfs.2013.11.002.
51. Horváth I, Van Beeck J, Merci B. Full-scale and reduced-scale tests on smoke movement in case of car park fire. Fire Saf J. 2013;57:35–43. doi:10.1016/j.firesaf.2012.10.009.
52. Occupational Safety and Health Administration (OSHA). Carbon monoxide poisoning. Washington, DC, USA: U.S. Department of Labor. 2022 [cited 2025 Jan 1]. Available from: https://www.osha.gov/sites/default/files/methods/osha-1026.pdf.
53. Henkes RAWM, Van Der Vlugt FF, Hoogendoorn CJ. Natural-convection flow in a square cavity calculated with low-Reynolds-number turbulence models. Int J Heat Mass Transf. 1991;34(2):377–88. doi:10.1016/0017-9310(91)90258-G.
54. Awbi HB. Ventilation of buildings. 1st ed. London, UK: Routledge; 1991. doi:10.4324/9780203476307.
55. Patankar SV. Numerical heat transfer and fluid flow. New York, NY, USA: Hemisphere Publishing; 1980. doi:10.1201/9781482234213.
56. Xamán J, Gijón-Rivera M. Dinámica de fluidos computacional paraingenieros. Bloomington, Indiana: Palibrio; 2016. 236 p.
57. Nielsen PV. Specification of a two-dimensional test case. Energy conservation in buildings and community system. In: Annex 20. Aalborg, Denmark: Institut for Bygningsteknik, Aalborg Universitet; 1990. p. 15.
58. Lage JL, Bejan A, Anderson R. Removal of contaminant generated by a discrete source in a slot ventilated enclosure. Int J Heat Mass Transf. 1992;35(5):1169–80. doi:10.1016/0017-9310(92)90177-T.